Theoretical and Experimental Description for a Radial Supersonic Flowfield

N. L. Rapagnani*
U.S. Air Force Weapons Laboratory, Kirtland Air Force Base, New Mexico
and
F. R. Zumpano†
United Technologies Research Center, East Hartford, Connecticut

A time-dependent, two-dimensional viscous analysis was employed to evaluate the radially expanding supersonic flowfield created by a cylindrical ring-type source nozzle. This complex flowfield is similar to that generated by a line source with oblique shock waves, expansion fans, and embedded wake regions. Comparisons are made between analytical and experimental results for a source-flow nozzle having an exit Mach number of approximately two and using air on the flowing gas. The analytical results are in excellent agreement with the experimentally measured pitot and static pressure distributions obtained parallel to the source-nozzle axis at different radial locations.

Nomenclature

E = internal energy
K = thermal conductivity
P = pressure, Eq. (5)
q_r, q_x = heat flux components, Eq. (4)
r = radial dimension
t = time
u = axial velocity
v = radial velocity
x = axial dimension
ρ = density
γ = ratio specific heats
$\sigma_{rr}, \sigma_{\theta\theta}, \sigma_{xx}, \tau_{rx}$ = stress tensors, Eq. (3)
μ = first viscosity coefficient
λ = second viscosity coefficient

Subscripts

AA = area averaging
ST = stream-thrust averaging

Introduction

UNDERSTANDING the characteristics of the flowfield at the entrance to a supersonic diffuser is critical for the design of a short-length diffuser capable of high-pressure recovery. Analytical and experimental techniques were developed years ago for the evaluation of the internal supersonic flows produced by axisymmetric and two-dimensional nozzles. These techniques are employed to determine diffuser inlet conditions for the design of linear-flow (axisymmetric and two-dimensional) supersonic diffusers. Similar techniques would be useful for the design of radial-flow supersonic diffusers. To date, very little work has been reported on the evaluation of the flowfield generated by a supersonic source-flow nozzle. The purpose of this paper is to describe a comparison of analytical and experimental results for the flowfield of such a nozzle.

A supersonic source nozzle generates a radially expanding flowfield as if from a theoretical line source. Finitude requires that such a nozzle have a cylindrical geometry in which the nozzle fluid supply enters through the ends of the cylinder and the nozzle effluent exits through the cylindrical surface. The structure of the nozzle may take different forms within the confines of this cylindrical volume. A series of nozzle rings comprise the structural form of interest herein.

Past investigations of radial-flow source nozzles were associated with the possible application of this nozzle concept to high-power laser systems. Analytical and experimental investigations of radial-flow supersonic nozzles were first conducted by AVCO.[1] The objective of their investigation was to determine the stability of a normal shock in a radially expanding supersonic flowfield. Theoretical analysis predicted that a supersonic source flow could be terminated by a stable cylindrical normal shock. Experimentally, it was found that a cylindrical normal shock was unattainable, because an axially uniform supersonic flow could not be established due to flow separations from the walls of the gas flow collector duct. This work utilized source nozzle hardware that had a relatively low length-to-diameter ratio of 0.18. Investigations conducted at the U.S. Air Force Flight Dynamics Laboratory[2,3] utilized source nozzles with higher length-to-diameter ratios (0.69 and 2.85) in an effort to minimize the effects of the end-wall separation phenomenon. Here, a centrally located high-pressure feed tube was employed to modify the maldistribution problem inherent as the nozzle length-to-diameter ratio is increased. However, as with the lower length-to-diameter ratio nozzle of Ref. 1, end-wall separation problems still prevented the establishment of an axially uniform radial flowfield. This problem was overcome in the work done at United Technologies Research Center,[4,5] where flow energization techniques were employed to prevent flow separation from the end-wall surfaces. A fully supersonic radial flowfield was established with good axial uniformity. Measurements of pitot and static pressure distributions were made by probing the supersonic flowfield and Schlieren flow visualization techniques were employed to photograph the flowfield.

Experimental and analytical results are compared herein to determine the efficiency of using an existing computational fluid dynamic code[6] to evaluate the complex flowfield conditions generated by a supersonic-flow source nozzle. The com-

---

Received Aug. 30, 1985; revision received March 18, 1986.

*Chief, Fluid Mechanics Branch. Member AIAA.

†Senior Research Engineer, Propulsion Technology. Member AIAA.

putational procedure employed for these flowfield calculations is briefly described herein. Subsequently, the source nozzle geometry, test procedures, and experimental conditions are described. This is followed by discussion of the results and comparisons of the calculated flowfield parameters with test data.

Numerical Model

The capabilities of the RAVEN numerical code have been presented previously.[6] The RAVEN code represents an innovative methodology for the construction of a numerical analogy of the governing partial differential equations of continuum mechanics. The equations are solved using finite element theory, while nodal analogs are employed to allow the use of finite difference techniques for numerical integration. Thus, it combines geometrical information of finite element theory with the simplicity of finite difference techniques. The best features of both theories are employed and a very efficient means of solving the flow equations with general hexahedral-shaped elements evolved. This technique allows for complex geometries to be handled in finite element methodology while solutions are obtained from finite difference analogs. With all of the element information available for finite differencing, the method yields rapid and accurate solutions to very difficult flowfields containing complex boundaries.

The form of the Navier-Stokes equations solved by the RAVEN code for this study are presented below.

Continuity:

$$\frac{\partial\rho}{\partial t}+\frac{\partial(\rho u)}{\partial x}+\frac{1}{r}\,\frac{\partial(\rho v r)}{\partial r}=0 \tag{1}$$

Conservation of momentum, x direction:

$$\frac{\partial(\rho u)}{\partial t}+\frac{\partial(\rho u^2)}{\partial x}+\frac{1}{r}\,\frac{\partial(\rho u v r)}{\partial r}$$

$$=\frac{-\partial p}{\partial x}-\left[\frac{1}{r}\,\frac{\partial}{\partial r}(r\tau_{rx})+\frac{\partial}{\partial x}(\sigma_{xx})\right] \tag{2}$$

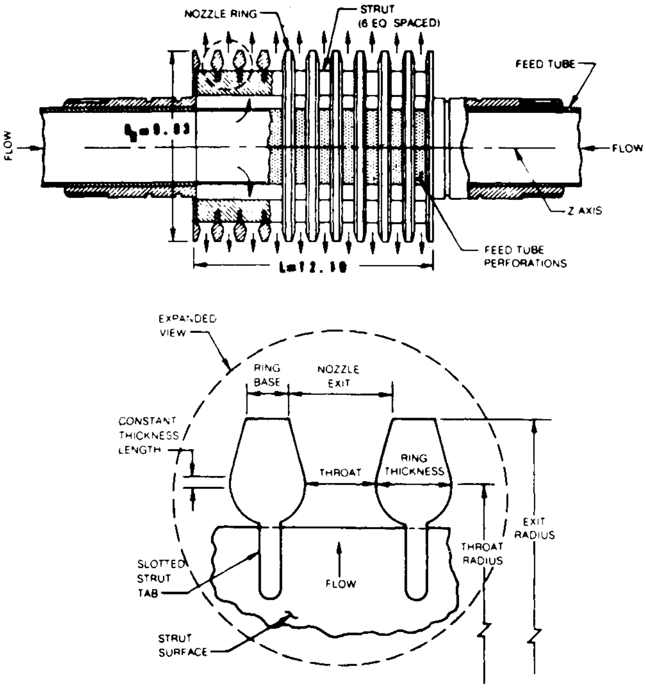

Fig. 1 Source-flow nozzle.

Conservation of momentum, r direction:

$$\frac{\partial(\rho v)}{\partial t}+\frac{\partial}{\partial x}(\rho u v)+\frac{1}{r}\,\frac{\partial}{\partial r}(\rho v^2 r)$$

$$=\frac{-\partial p}{\partial r}-\left[\frac{1}{r}\,\frac{\partial}{\partial r}(r\sigma_{rr})-\frac{\sigma_{\theta\theta}}{r}+\frac{\partial\tau_{rx}}{\partial x}\right] \tag{3}$$

where the viscous stress tensor components are given by

$$\sigma_{rr}=-\left[2\mu\cdot\frac{\partial v}{\partial r}+\lambda\left(\frac{1}{r}\,\frac{\partial}{\partial r}(rv)+\frac{\partial u}{\partial x}\right)\right]$$

$$\sigma_{\theta\theta}=-\left[2\mu\cdot\frac{v}{r}+\lambda\left(\frac{1}{r}\,\frac{\partial}{\partial r}(rv)+\frac{\partial u}{\partial x}\right)\right]$$

$$\sigma_{xx}=-\left[2\mu\cdot\frac{\partial u}{\partial x}+\lambda\left(\frac{1}{r}\,\frac{\partial}{\partial r}(rv)+\frac{\partial u}{\partial x}\right)\right]$$

$$\tau_{rx}=-\mu\left(\frac{\partial u}{\partial r}+\frac{\partial v}{\partial x}\right)$$

Here the first and second viscosity coefficients are μ and λ, respectively. Using Stokes' hypothesis, λ is the equal to $-(\tfrac{2}{3}\mu)$.

Conservation of energy:

$$\frac{\partial(\rho E)}{\partial t}+\frac{\partial}{\partial x}(\rho u E)+\frac{1}{r}\,\frac{\partial}{\partial r}(\rho v r E)$$

$$=-P\left[\frac{\partial}{\partial x}+\frac{1}{r}\,\frac{\partial u}{\partial r}(vr)\right]-\left[\frac{1}{r}\,\frac{\partial}{\partial r}(rq_r)+\frac{\partial(q_x)}{\partial x}\right]$$

$$-\frac{1}{r}\,\frac{\partial}{\partial r}[\sigma_{rr}vr+\tau_{rx}ur]-\frac{\partial}{\partial x}(\tau_{rx}v+\sigma_{xx}u) \tag{4}$$

where the heat flux components are given by

$$q_r=-K\frac{\partial T}{\partial r}\quad\text{and}\quad q_x=-K\frac{\partial T}{\partial x}$$

These equations are supplemented with the equation of state,

$$p=(\gamma-1)\rho E \tag{5}$$

These equations were used to treat two-dimensional, axisymmetric flows in a time-marching fashion using nodal analogs corresponding to MacCormack's two-step explicit method. A description of the computational domain employed for this analysis is presented in the results section below.

Source-Flow Nozzle Experiments

Experiments were conducted to determine the characteristics of the flowfield produced by a ring-type source-flow nozzle. Axial pitot and static pressure distributions were measured at selected circumferential and radial locations. Schlieren flow visualization data were recorded on 16 mm movie (at 100 frames/s) and 35 mm still film for selected test conditions. Detailed information about the experiment can be found in Ref. 5; a brief description of the experimental apparatus and some of the test results is provided herein.

The ring-type source nozzle consisted of an array of individual nozzle elements formed by rings arranged as shown in Fig. 1. The rings were connected by six axial struts to form a cylindrical structure with an overall length-to-diameter ratio of 1.24. Dimensional details of the source nozzle are contained in Fig. 2. A feed tube was located within this ring structure as illustrated in Fig. 1. The feed tube delivered flow axially to the annular region between the feed tube and nozzle ring elements via small holes in the feed walls. Thereafter, the flow generally moved in the radial direction and was captured by the gas-flow collector duct. This collector duct served as an exhaust plenum and was maintained at low pressure via a series of vacuum pumps.

The probe installation used to acquire pitot pressure distributions is shown in Fig. 3. A dual pitot-probe rake is illustrated, but this probe could be exchanged for a static pressure probe. The geometries of these probes are described in Fig. 4. A motorized drive mechanism was used to translate the installed probe in the axial direction across the flowfield from one end wall to the other. These axial traverses were made at the nozzle exit plane and at other selected radius ratios (r_p/r_N); see Fig. 2 at the 1.12 and 1.24 r_N locations.

During a test run, the pressure probe (pitot rake or static probe) was slowly translated (0.07 cm/s) parallel to the source nozzle axis as the probe pressure and position were recorded for approximately 200 data points. Four to six of these runs were necessary to obtain probe data for the entire axial length of the nozzle. The recorded data were analyzed to obtain local Mach number distributions, average pitot pressures, average static pressures, and average Mach numbers.

Axial pitot pressure profiles for each of the pitot probes (Fig. 3) can be seen in Fig. 5. These profiles were constructed by combining the data from several individual runs as indicated in this figure. The pressure distributions for the two probes do not overlap near the ends of the axial profiles due to an offset of 1.9 cm between the probes. Excellent agreement is indicated for the data from the two probes. This is also demonstrated by the pressure profiles in Fig. 6. Here, the digital data used to construct the pressure profiles in Fig. 5 were combined to produce a single combined-probe pressure profile. The data symbols have been eliminated in Fig. 6b and straight-line segments connect the digital data points to clarify the pressure distribution. Comparison of Fig. 6b with Fig. 6a shows that a sufficient number of data points were taken to clearly define the pitot pressure distribution. A static pressure probe was used in place of the pitot probe rake to obtain the axial static pressure distributions using a similar data acquisition technique.

All of the experimental data were acquired with the source-nozzle flowing air near the design point of 2.26 kg/s at a total temperature of about 300 K. The collector duct exhaust plenum pressure was maintained at about 85 Torr.

A summary of the average values calculated from the experimentally determined axial pressure distributions is shown in Table 1 for various radial locations (r_p/r_N) within the supersonic source flowfield. (Note that static pressure distributions were acquired at radial positions $r_p/r_N = 1.12$ and 1.24.) Only small differences resulted in the average parameters by using different averaging techniques, i.e., area averaging (AA) vs stream-thrust (ST) averaging. These data are included herein to provide quantitative information on the global characteristics of the flowfield generated by this source nozzle, although these data are not directly used in the subsequent comparisons with theoretical results.

Discussion of Results

A conceptual representation of the flowfield from a supersonic source-flow nozzle (without a diffuser in place) can be seen in Fig. 7. The radial extent of the supersonic flowfield could be controlled by varying the back pressure in the gas flow collector duct. Typically, the supersonic flowfield was terminated by a relatively uniform cylindrical normal shock, as illustrated in this figure.

Table 1 Average source-flow nozzle parameters

Parameter	Value		
r_p/r_N	1.0	1.12	1.24
$P_{P(AA)}$, Torr	259	232	207
$P_{S(AA)}$, Torr	—	28.7	23.7
$M_{(AA)}$	—	2.59	2.61
$M_{(ST)}$	—	2.52	2.55
$P_{P(ST)}$, Torr	—	255	204
$P_{S(ST)}$, Torr	—	25.9	23.1

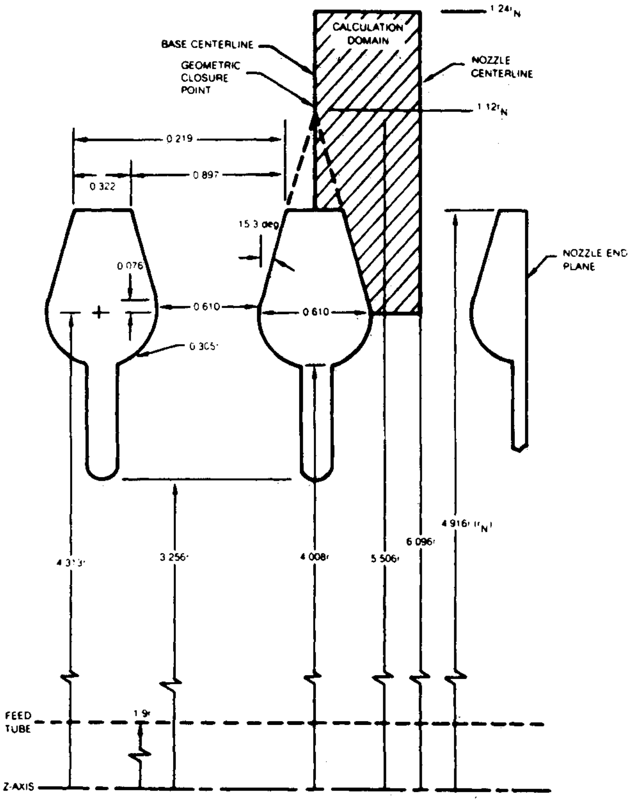

Fig. 2 Source flow nozzle geometry (total of 10 elements; dimensions in centimeters).

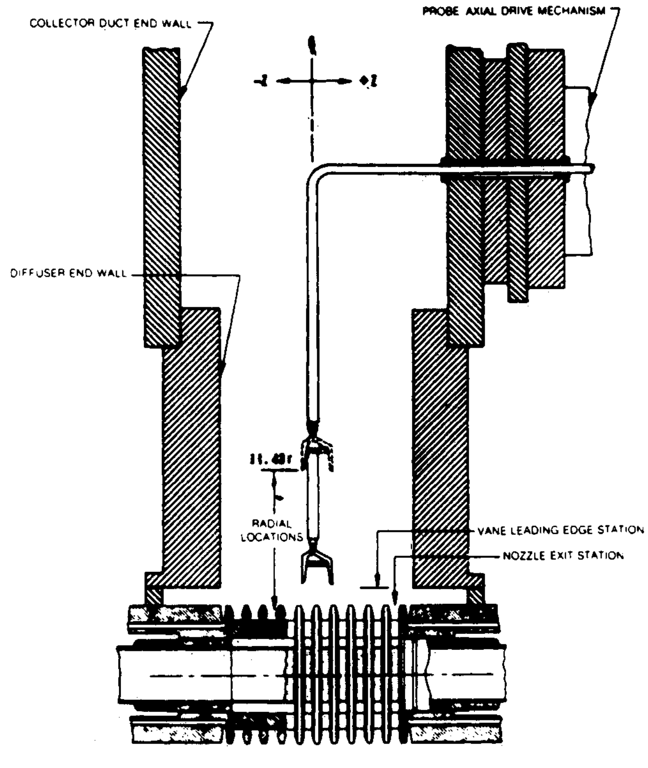

Fig. 3 Experimental configuration.

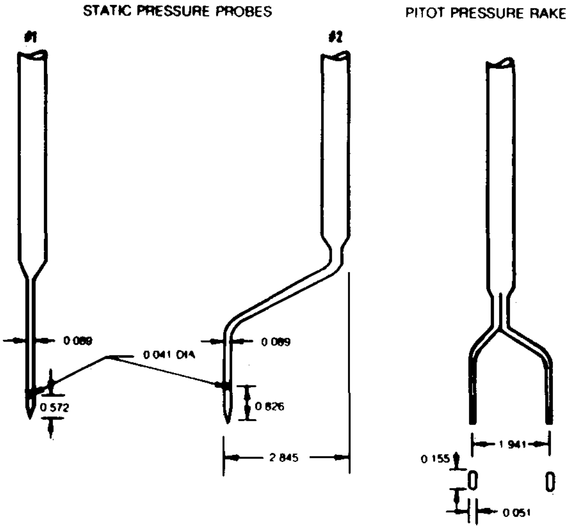

Fig. 4 Probe geometry (dimensions in centimeters).

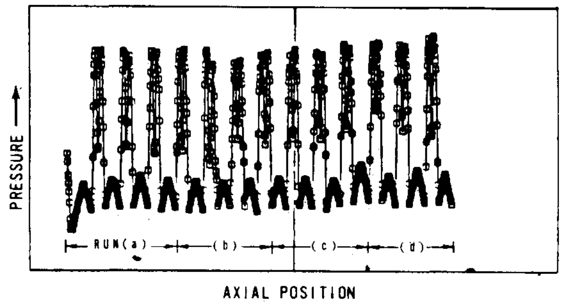

a) Probe 1.

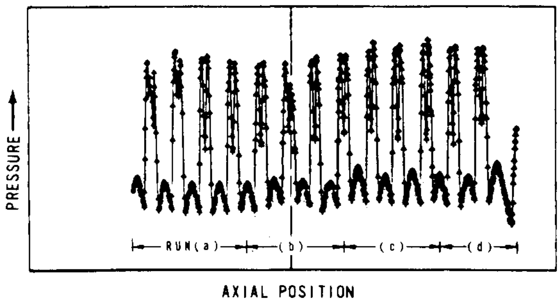

b) Probe 2.

Fig. 5 Typical pressure profile data (acquired with pitot probe rake). Note: all data acquired by translating dual-probe rake parallel to nozzle axis; axial offset between probes of 1.9 cm.

A schlieren photograph (1μs exposure) of such a flowfield with the knife edge oriented parallel to the nozzle axis can be seen in Fig. 8. The nozzle axis is horizontal at the center of the silhouette in this photograph. The rings of the source nozzle are clearly visible as the vertical nubs of the silhouette. These rings formed a bank of the 10 individual nozzle elements described in Fig. 1. This nozzle array was bounded in the axial direction by supersonic bank-blower nozzles as illustrated in Fig. 3 and are visible adjacent to each end wall. The bank-blower nozzles provided high-momentum flow adjacent to the walls of the gas flow collector duct to reduce the extent of end-wall flow separation. The flow is radial from the nozzle axis, but appears to be in the vertical direction as a consequence of the two-dimensionality of the photograph. This image is representative of integrated variations in the density gradient encountered by the collimated light rays passing through the

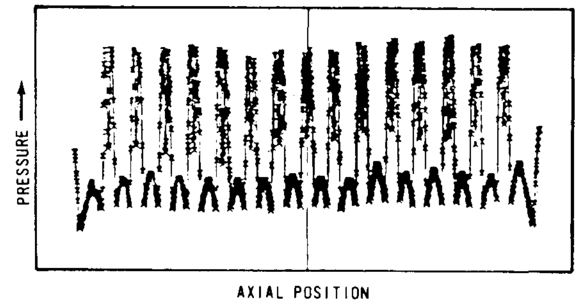

a) Data symbols included.

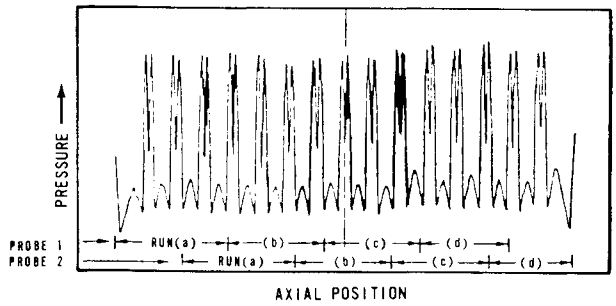

b) Data symbols eliminated.

Fig. 6 Typical pitot pressure profiles, combined data.

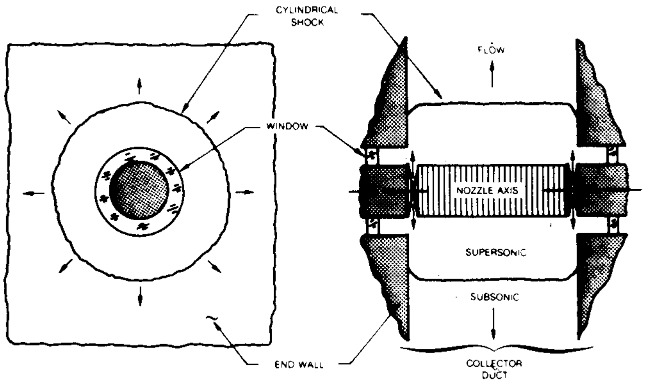

Fig. 7 Cylindrical normal shock in a supersonic flowfield.

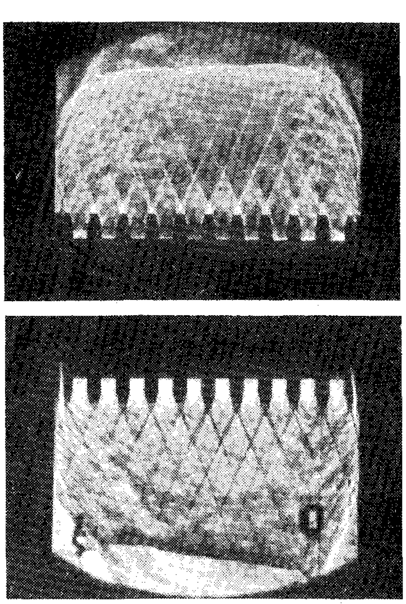

Fig. 8 Schlieren photo of entire flowfield.

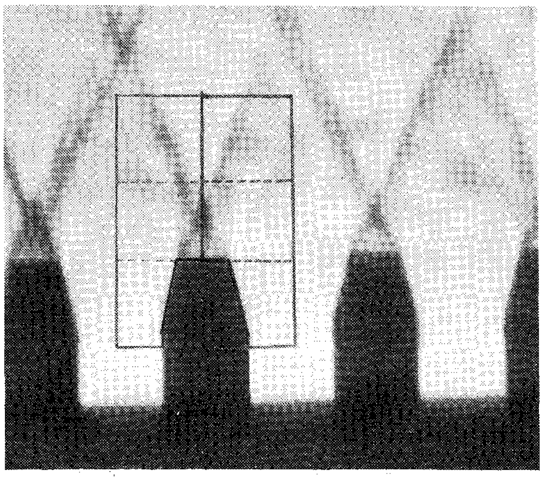

Fig. 9 Enlargement of schlieren photo.

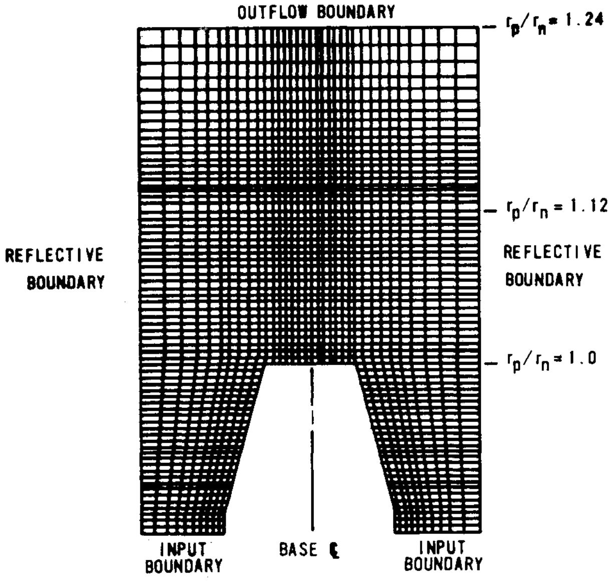

Fig. 10 Grid used in calculational domain.

cylindrical flowfield, in contrast to a purely sectional view of the flowfield. A stable cylindrical or barrel-type normal shock is featured in Fig. 8. The stability of the shock was ascertained from high-speed schlieren movies. This shock encompasses the entire supersonic flowfield from one end wall to the other in the gas flow collector duct. The supersonic flowfield in Fig. 8 is initiated at the upstream end of the expansion provided by the tapered width of the source-nozzle rings (refer to ring/throat location in Fig. 1). From a sonic condition at the throat, the flow expands in both the radial and axial directions toward the exit diameter of the source nozzle. At the nozzle exit, the flow expands more rapidly in the axial direction and is seen to fill the void behind the base regions of the nozzle rings. A photographic enlargement of this region can be seen in Fig. 9. Slightly downstream of the exit diameter of the source nozzle, flows from the adjacent nozzle elements interact, giving rise to turnback shocks that eliminate axial expansion of the flow by turning it back to the purely radial direction. (These turnback shocks cause the diamond-shaped patterns upstream of the cylindrical normal shock in Fig. 8.) The multiple waves and the relatively thick appearance of the turnback shocks in Fig. 9 is probably a result of out-of-plane density gradients caused by the light rays passing through the cylindrical flowfield, as seen in Figure 7. The extent of the recirculation region downstream of the nozzle rings is also clearly evident in this photograph.

The computational domain employed in the numerical analysis of the flowfield is shown as a cross-hatched area in Fig. 2 and illustrated in Fig. 9 replicated about the nozzle/ring/base centerline. (The radial location $r_p/r_N = 1.0$, 1.12, and 1.24, where the axial pressure distributions were also measured can be seen in Fig. 9.) The finite element grid within this domain is shown in Fig. 10. The flow across the input boundary of the computational domain (lower boundary in Fig. 10) was assumed uniform at sonic velocity conditions as it entered the computational domain, two-dimensional axisymetric within the domain and confined by reflective boundaries as it progressed, while expanding radially to the exit (the outflow boundary in Fig. 10) of the domain. The nozzle wall was a no-slip boundary with a constant wall temperature of 300 K. This condition is important in establishing a boundary layer near the wall, which influences the location and size of the separated region.

The calculated flowfield depicted by the velocity vectors in Fig. 11 can be compared to the schlieren photograph of the flowfield in Fig. 9. Note that in Fig. 11 the length of each arrow is proportional to the magnitude of the velocity and the orientation of the arrow indicates the local flow direction. The

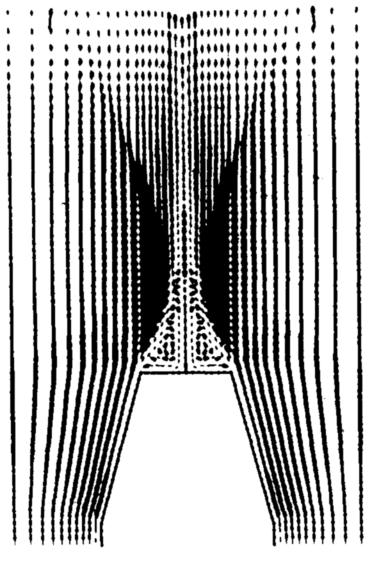

Fig. 11 Velocity vectors, $V_{\max} = 63{,}746.30$.

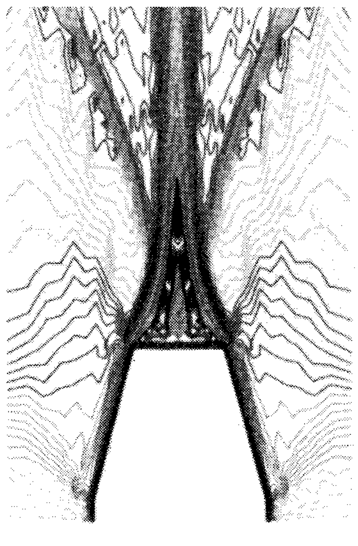

Fig. 12 Mach number contours.

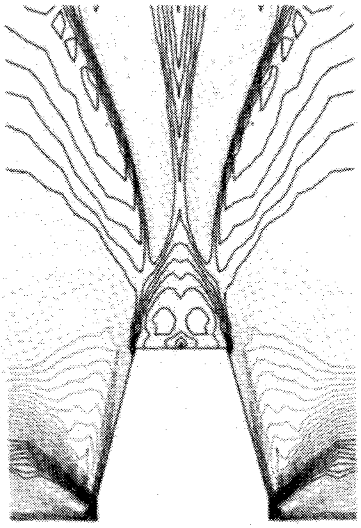

Fig. 13 Density contours.

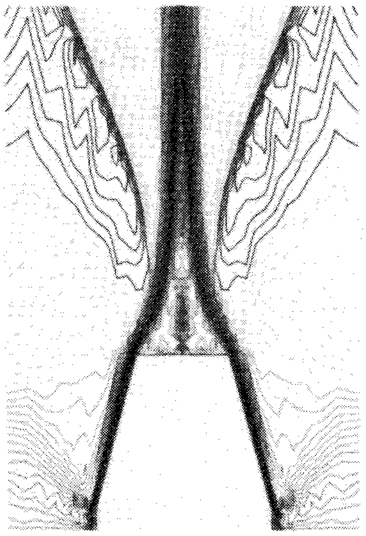

Fig. 14 Temperature contours.

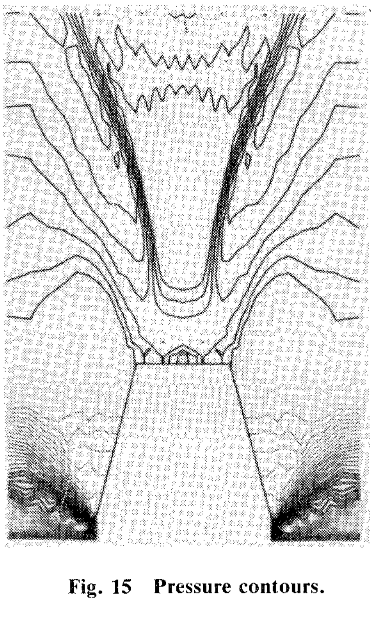

Fig. 15 Pressure contours.

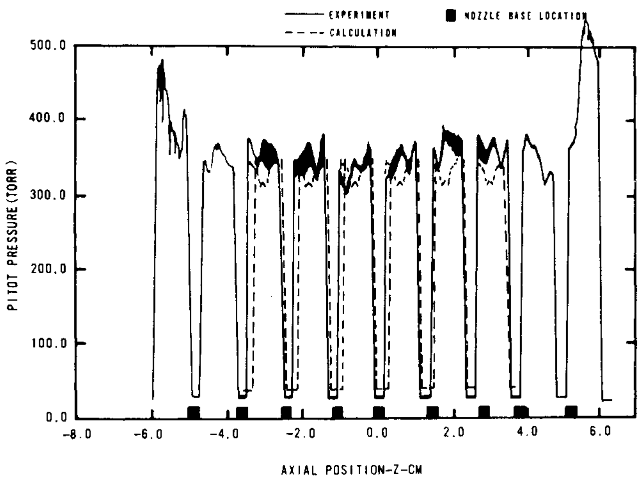

Fig. 16 Pitot pressure distributions ($r_p/r_n = 1.0$), experiment vs theory.

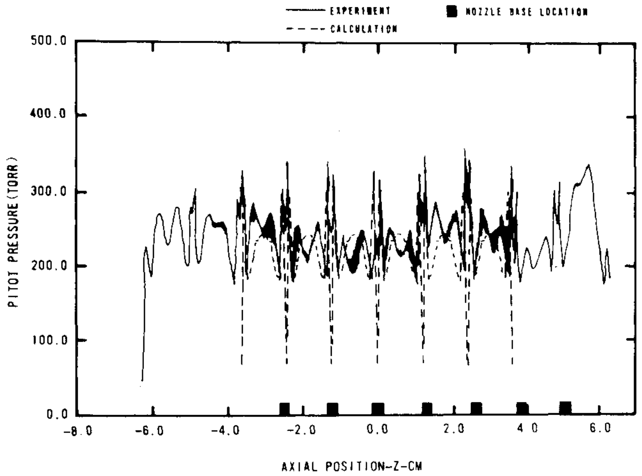

Fig. 17 Pitot pressure distributions ($r_p/r_n = 1.12$), experiment vs theory.

flowfield features depicted by the velocity vectors are in excellent agreement with those in the photograph. The recirculation zone downstream of the ring base is of similar relative size and location in both figures. Abrupt turning of the flow clearly locates the turnback shocks in the velocity vector plot. These theoretical shock locations are in good agreement with the actual shock locations shown in Fig. 9. Similar flow features can be seen in the calculated contour plots of Mach number, density, temperature, and pressure in Figs. 12-15, respectively. In these figures, the contours are presented as 50 equally spaced curves between the minimum and maximum value of each variable.

Axial pitot pressure, static pressure, and Mach number distributions were determined across the computational domain at radial locations selected to match those of the experimental results. These distributions were replicated for each nozzle element to create complete distributions for the axial width of the source nozzle tested in Ref. 5. A comparison of these analytical results with the experimental results reported in Ref. 5 can be made from observation of Figs. 16-22.

Axial pitot pressure distributions are contained in Figs. 16-18 for three radial locations, $r_p/r_N = 1.0$, 1.12, and 1.24, respectively. At the nozzle exit radius (Fig. 16), excellent agreement is featured between the analytical and experimental results. Both show that the pitot pressures just downstream of the nozzle base regions are at a uniformly low level close to the measured base static pressure, while the pitot pressures in the

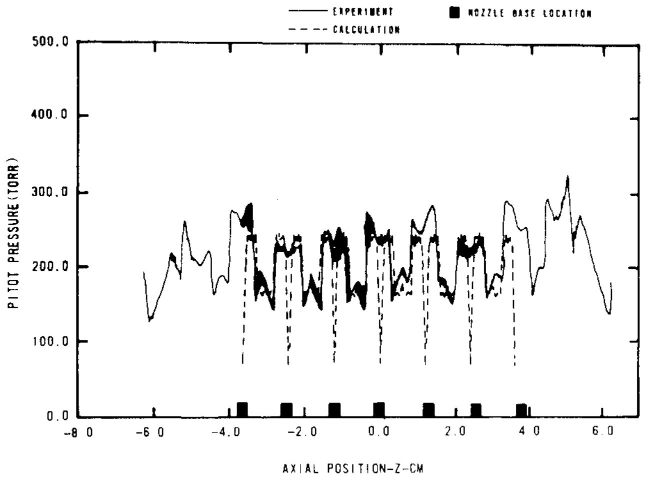

Fig. 18 Pitot pressure distributions ($r_p/r_n = 1.24$), experiment vs theory.

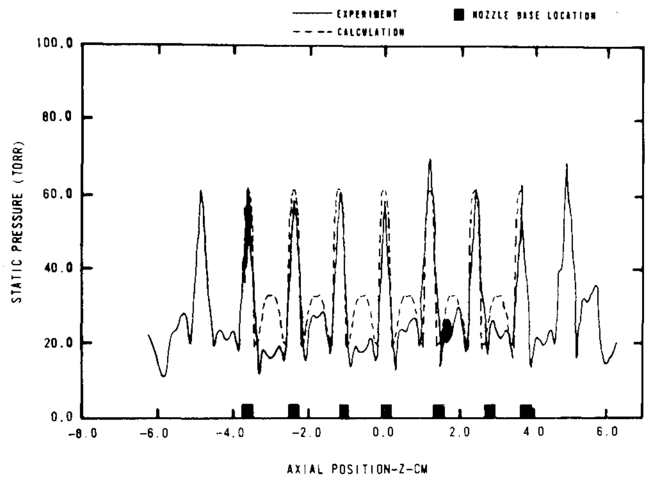

Fig. 19 Static pressure distributions ($r_p/r_n = 1.12$), experiment vs theory.

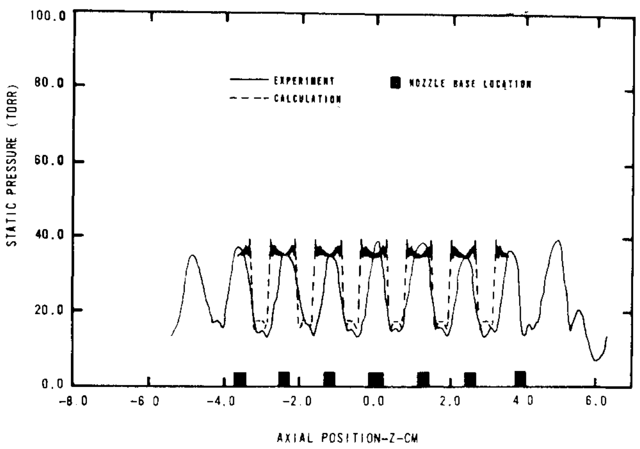

Fig. 20 Static pressure distributions ($r_p/r_n = 1.24$), experiment vs theory.

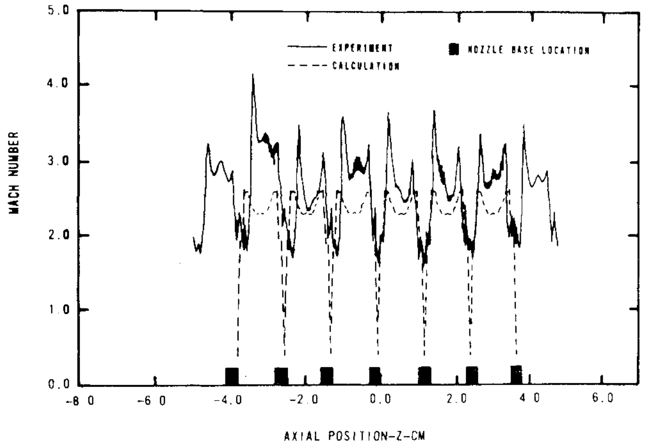

Fig. 21 Mach number distributions ($r_p/r_n = 1.12$), experiment vs theory.

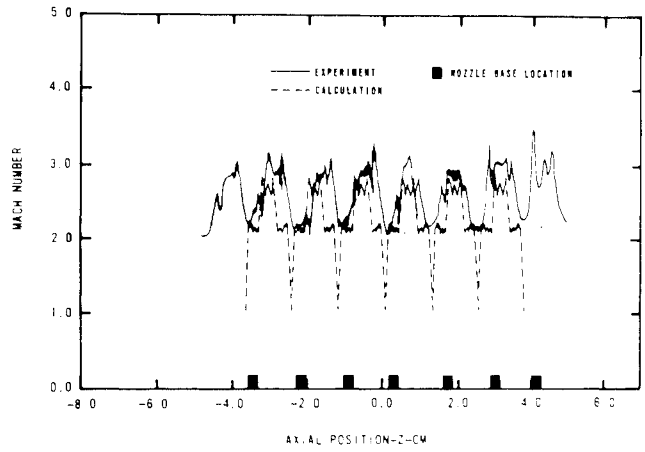

Fig. 22 Mach number distributions ($r_p/r_n = 1.24$), experiment vs theory.

core-flow regions are at relatively higher levels. Downstream of the nozzle exit at radius ratios of 1.12 (Fig. 17) and 1.24 (Fig. 18), the good correspondence of the analytical and experimental results is interrupted only in a narrow region downstream of the ring base centerlines. Here, the analytically determined pitot pressure is much lower than the measured pitot pressure. The analytical value results from a viscous wake region that persists downstream of the base recirculation zone. This narrow wake region may not have been observed experimentally due to the size of the probe tip (see Fig. 4), slight axial vibration of the probe tip, and/or slight axial instability of the wake region—all of which would tend to average the measured pressure in regions of strong gradients. The high pitot pressures adjacent to this wake region at radius ratios of 1.12 and 1.24 are a result of flow compression due to the turnback shocks; see Fig. 9.

Axial static pressure distributions are contained in Figs. 19 and 20 for two radial locations, $r_p/r_N = 1.12$ and 1.24, respectively. The correspondence of these analytical and experimental results is remarkable when the difficulty of making accurate measurements with a static pressure probe in a complicated supersonic flowfield is considered. Some of the differences between the analytical and experimental results are caused by a slight pneumatic lag in the static probe pressure measurement resulting from the translation of the probe through the varying pressure environment as the data were acquired. Additionally, the probe tip upstream of the static pressure orifice probably disrupted the flowfield more than would be expected in a uniform flowfield. (Here, the probe was traversed through a complex flow with embedded oblique shockwaves, expansion fans, and shear layers.) Static pressure maxima are generally centered on the nozzle/ring bases at both radial locations; see Figs. 19 and 20. The magnitude of the analytically determined peak static pressure is in excellent agreement with the experimental measurements; the axial width of the pressure peaks is calculated to be greater than measured.

Both analytical and experimental determined Mach number distributions were compared for radius ratios of 1.12 and 1.24; see Figs. 21 and 22, respectively. The comparison between the analytical and experimental results is generally good, except in the narrow viscous wake region downstream of the source/nozzle rings. Here again, the details of the wake region may have been lost in the experimental results due to the finite size of the pressure probes and the previously mentioned complications associated with the static pressure measurement.

Conclusions

The RAVEN computational model has been used to calculate the flowfield generated by supersonic ring-type source nozzles. The characteristics of the radial flowfield (including shock waves, wakes, and recirculation zones) are accurately predicted by this calculation procedure. The analysis was shown to shed new understanding to the experimental results, because the resolution in the grid used by the numerical model was much finer than could be experimentally measured. Further applications of this code to alternative source/nozzle designs should permit a more complete understanding of supersonic source flows.

References

[1] "Cylindrical Gas Dynamics Lasers," AFWL-TR-74-5, June 1984.

[2] Howard, J.M. and Hasinger, S.H., "Diffusion Characteristics of Large L/D Radial Outflow Nozzle Systems, Laser Digest," AFWL-TR-75-229, Oct. 1975.

[3] Hasinger, S.H., "Analysis and Design of a Supersonic Radial Outflow System," AFWAL-TR-80-3028, Oct. 1980.

[4] Zumpano, F.R., Guile, R.N., and Eckerle, W.A., "Supersonic Radial-Flow Diffuser Investigations," United Technologies Research Center, East Hartford, CT, April 1980.

[5] Zumpano, F.R., Haas, M., Guile, R.N., and Sobel, D.R., "Radial-Flow Diffuser Technology Program," AFWL-TR-84-81, Dec. 1984.

[6] Hendricks, W.L. et al., "RAVEN: A Computer Code for the Solution to the Time-Dependent, Three-Dimensional Navier-Stokes Equations with Non-Equilibrium Chemistry, Laser Gain, and Turbulence," AFWL-TR-81-184, April 1983.